MNRAS 000, 1–13 (20XX) Preprint 10 November 2015 Compiled using MNRAS LATEX style file v3.0

Doppler-imaging of the planetary debris disc at the white dwarf SDSS J122859.93+104032.9

Christopher J. Manser [1]★, Boris T. Gänsicke [1], Thomas R. Marsh [1], Dimitri Veras [1], Detlev Koester [2], Elmé Breedt [1], Anna F. Pala [1], Steven G. Parsons [3], John Southworth [4]

[1] *Department of Physics, University of Warwick, Coventry CV4 7AL, UK*
[2] *Institut für Theoretische Physik und Astrophysik, University of Kiel, 24098 Kiel, Germany*
[3] *Departamento de Física y Astronomía, Universidad de Valparaíso, Avenida Gran Bretana 1111, Valparaíso, Chile*
[4] *Astrophysics Group, Keele University, Staffordshire, ST5 5BG, UK*

arXiv:1511.02230v1 [astro-ph.SR] 6 Nov 2015

Accepted 20XX. Received 20XX; in original form 20XX

ABSTRACT

Debris discs which orbit white dwarfs are signatures of remnant planetary systems. We present twelve years of optical spectroscopy of the metal-polluted white dwarf SDSS J1228+1040, which shows a steady variation in the morphology of the 8600 Å Ca II triplet line profiles from the gaseous component of its debris disc. We identify additional emission lines of O I, Mg I, Mg II, Fe II and Ca II in the deep co-added spectra. These emission features (including Ca H & K) exhibit a wide range in strength and morphology with respect to each other and to the Ca II triplet, indicating different intensity distributions of these ionic species within the disc. Using Doppler tomography we show that the evolution of the Ca II triplet profile can be interpreted as the precession of a fixed emission pattern with a period in the range 24–30 years. The Ca II line profiles vary on time-scales that are broadly consistent with general relativistic precession of the debris disc.

Key words: Stars: individual: SDSS J122859.93+104032.9 – white dwarfs – Circumstellar matter – accretion, accretion discs – line: profiles.

1 INTRODUCTION

The first discovery of a debris disc around a white dwarf was made by Zuckerman & Becklin (1987) via the detection of an infrared excess at G29–38, which was later interpreted as the emission from circumstellar dust by Graham et al. (1990). This disc is thought to be the result of the tidal disruption of an asteroid or comet within a remnant planetary system that survived the main sequence evolution of the white dwarf progenitor (Jura 2003; Debes et al. 2012; Veras et al. 2014). Since the discovery of infrared emission from G29–38, debris discs have been detected at more than thirty additional white dwarfs (Kilic et al. 2006; Farihi et al. 2008, 2009; Jura et al. 2009; Debes et al. 2011; Hoard et al. 2013; Bergfors et al. 2014; Rocchetto et al. 2015), which are in all (but possibly one, see Xu et al. 2015) cases accompanied by the detection of trace metals in the white dwarf photosphere (Koester et al. 1997; Zuckerman et al. 2007; Jura & Young 2014).

Two decades after the discovery of dust at G29–38, Gänsicke et al. (2006) identified a gaseous disc around the white dwarf SDSS J122859.93+104032.9 (henceforth SDSS J1228+1040) via the detection of double peaked emission lines of Ca II at 8498.02 Å, 8542.09 Å, 8662.14 Å, (henceforth the Ca II triplet), which is indicative of Keplerian rotation in a flat disc (Horne & Marsh 1986). *Spitzer* and *HST* follow-up observations detected circumstellar dust and a plethora of metallic absorption lines, respectively; strengthening the connection of the gaseous material to the presence of a remnant planetary system around this white dwarf (Brinkworth et al. 2009; Gänsicke et al. 2012). The morphology of these emission lines provided firm dynamical confirmation that the debris disc resides within the tidal disruption radius of the white dwarf.

Despite intense searches over the last decade, gaseous discs have been found around only seven white dwarfs (Gänsicke et al. 2006, 2007, 2008; Gänsicke 2011; Farihi et al. 2012; Melis et al. 2012; Wilson et al. 2014). All seven also exhibit infrared excess from dusty discs, five of which were discovered after their gaseous counter-

★ E-mail: C.Manser@warwick.ac.uk

© 20XX The Authors

part (Dufour et al. 2010; Brinkworth et al. 2012). Only in HE 1349–2305 and SDSS J095904.69–020047.6 (henceforth SDSS J0959–0200) were the Ca II emission lines detected after the initial discovery of a dusty disc. Only a small fraction of the systems hosting a dust-dominated debris disc also have an observable gaseous component, implying that the presence of detectable amounts of gas is not inherent to the presence of a debris disc.

The origin of these seven gaseous discs is still unclear. Several scenarios have been proposed, including runaway feedback between sublimation and the ensuing gas drag on the dust, leading to a rapid increase in the accretion rate onto the white dwarf (Rafikov 2011; Metzger et al. 2012), and secondary impacts of asteroids on an existing debris disc (Jura 2008). Both cases involve dynamic interactions in the disc which might lead to detectable levels of variability.

Changes in the strength and morphology of the Ca II triplet have been reported in a number of systems. SDSS J161717.04+162022.4 (Wilson et al. 2014, henceforth SDSS J1617+1620) was identified to host a transient gaseous disc, which following its first detection monotonically decreased in strength over eight years until it dropped below detectability. In contrast SDSS J084539.17+225728.0 (Gänsicke et al. 2008; Wilson et al. 2015, henceforth SDSS J0845+2257) shows changes in the morphology of the Ca II triplet, but not in the strength of the lines. We also note that SDSS J0959–0200 has shown a large decrease in the infrared emission from the dusty component of the debris disc, however no time-resolved observations of the gaseous disc have been published (Farihi et al. 2012; Xu & Jura 2014).

We have been spectroscopically monitoring the white dwarf SDSS J1228+1040 for twelve years and report in this paper pronounced changes in the morphology of the Ca II triplet. We also show the first intensity map in velocity space of the Ca II gas at SDSS J1228+1040 using Doppler tomography.

2 OBSERVATIONS

2.1 The data

We obtained optical spectroscopy of SDSS J1228+1040 from 2003 to 2015 with several instruments: X-shooter (Vernet et al. 2011) and the Ultraviolet and Visual Echelle Spectrograph (UVES, Dekker et al. 2000) which are both on the ESO Very Large Telescope (VLT); the 2.5 m Sloan Digital Sky Survey telescope (SDSS, data retrieved from DR7 and DR9, Gunn et al. 2006; Abazajian et al. 2009; Eisenstein et al. 2011; Ahn et al. 2014; Smee et al. 2013); and the Intermediate dispersion Spectrograph and Imaging System (ISIS) on the William Herschel Telescope (WHT). These observations are summarised in Table 1. The X-shooter and UVES data were reduced using the `REFLEX` [1] reduction work flow using the standard settings and optimising the slit integration limits (Freudling et al. 2013). The sky spectrum of each observation was used to determine the spectral resolution. We also report the parameters of SDSS J1228+1040 in Table 2. The first ISIS spectrum of SDSS J1228+1040 obtained on the WHT were reported in Gänsicke et al. (2006, 2007), the 2010 ISIS spectrum was obtained with a similar setup, and was reduced in the same fashion (see Farihi et al. 2012 and Wilson et al. 2014 for additional details).

[1] Documentation and software for `REFLEX` can be obtained from http://www.eso.org/sci/software/reflex/

2.2 Telluric corrections

The X-shooter observations (as with all ground-based spectroscopy) are affected by telluric lines, in particular around the Ca II triplet. We removed this contamination using 152 empirical telluric templates from the X-shooter library (XSL), provided by Chen et al. (2014). Each template includes the normalised telluric absorption features over the wavelength range 5300 – 10200 Å. The telluric absorption does not affect this entire range and hence we split the templates into seven smaller regions which we correct for independently. We first continuum normalise the observed spectrum and then we fit each of the seven regions to all 152 templates with two free parameters; a wavelength shift (for telescope flexure) and the intensity of the telluric features (which varies with the atmospheric conditions between different observations). The best-fitting template for each region is used to correct that part of spectrum. An example of a telluric corrected X-shooter spectrum for SDSS J1228+1040 is shown in Figure 1.

2.3 Velocity corrections

The observations of the Ca II triplet were converted from wavelength to velocity space using the rest wavelengths, 8498.02 Å, 8542.09 Å, 8662.14 Å, which are corrected for the systemic velocity, i.e. the velocity along the line of sight. Gänsicke et al. (2012) calculated a velocity difference of $+57 \pm 1\,\mathrm{km\,s^{-1}}$ between the photospheric absorption lines of the white dwarf and the interstellar ultraviolet absorption lines in SDSS J1228+1040. This value combines the systemic velocity as well as the gravitational red-shift of the photospheric absorption lines at the white dwarf surface (Koester 1987). Adopting a white dwarf mass and radius of $0.705\,\mathrm{M_\odot}$ and $0.01169\,\mathrm{R_\odot}$, respectively (Koester et al. 2014), we obtain a gravitational red-shift of $+38 \pm 4\,\mathrm{km\,s^{-1}}$, resulting in a systemic velocity of $+19 \pm 4\,\mathrm{km\,s^{-1}}$. This velocity is used to shift the Ca II triplet observations to the rest frame of the system as well as for Doppler Tomography discussed in Section 5. All the Ca II triplet observations are shown in velocity space in Figure 2 and we discuss the evolution of the Ca II triplet in the next section.

3 EVOLUTION OF THE CA II TRIPLET STRUCTURE

3.1 Double peaked emission from a disc

Horne & Marsh (1986) showed that a circular gaseous disc with a radially symmetric intensity distribution orbiting a central mass will produce symmetric double-peaked emission line profiles in velocity space (See Figure 1 of Horne & Marsh 1986), due to the range in velocities across the disc projected along the line of sight. Two properties

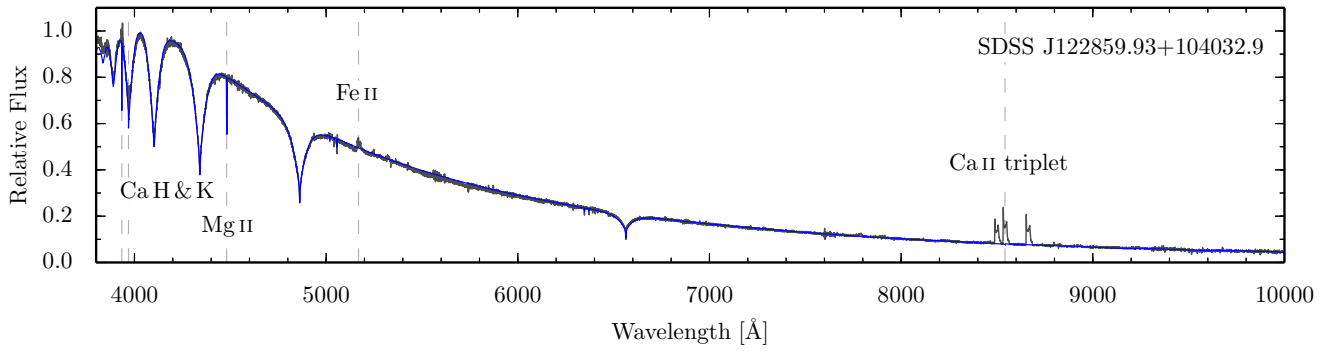

Figure 1. X-shooter spectra (grey) of SDSSJ 1228+1040 (obtained in January 2011) together with a model fit (blue) using the atmospheric parameters (Table 2). The strongest emission and absorption lines have been labelled.

Table 1. Log of observations of SDSS J1228+1040. [a] Different exposure times for the individual UVES arms (blue / red lower and upper) and X-shooter arms (UVB / VIS). [b] Observations did not cover the Ca II triplet. We did not use data collected by the NIR arm of X-shooter as the signal-to-noise ratio was too poor.

Date	Telescope/Instrument	Wavelength Range [Å]	Resolution [Å]	Total Exposure Time [s] [a]
2003 March 27	SDSS	3800 – 9200	2.7	2900
2006 June 30 - July 01	WHT/ISIS	7500 – 9200	2.0	12000
2007 April 07	VLT/UVES	3045 – 9463	0.19	11800 / 11360
2007 June 06	VLT/UVES	3758 – 9463	0.18	5900 / 5680
2007 July 09 - 10	VLT/UVES	3757 – 9463	0.18	5900 / 5680
2008 January 10	VLT/UVES	3759 – 9464	0.18	5900 / 5680
2008 April 11 [b]	VLT/UVES	3284 – 6649	0.13	11800 / 11360
2008 June 27	VLT/UVES	3758 – 9463	0.18	5900 / 5680
2008 July 19	VLT/UVES	3758 – 9463	0.18	5900 / 5680
2009 January 12 [b]	VLT/UVES	3284 – 6650	0.14	5900 / 5680
2009 February 03	VLT/UVES	3758 – 9464	0.18	5900 / 5680
2009 April 04	VLT/UVES	3282 – 9463	0.18	17700 / 17040
2010 April 27	WHT/ISIS	8100 – 8850	1.1	1800
2011 January 22	VLT/X-Shooter	2990 – 10400	1.09	2840 / 1400
2011 May 29	VLT/X-Shooter	2990 – 10400	1.14	2840 / 1400
2011 June 14	VLT/X-Shooter	2990 – 10400	1.09	2840 / 1400
2012 March 26	VLT/X-Shooter	2990 – 10400	1.11	2840 / 1400
2014 March 06	VLT/X-Shooter	2990 – 10400	1.10	1971 / 3045
2014 June 02	VLT/X-Shooter	2990 – 10400	1.09	1314 / 2030
2015 May 11	VLT/X-Shooter	2990 – 10400	1.10	2380 / 2510
2015 May 18	VLT/UVES	3732 – 9463	0.20	2980 / 2960

Table 2. Atmospheric parameters for SDSS J1228+1040 (from Koester et al. 2014).

$T_{\rm eff}$ [K]	log g	$M_{\rm WD}$ [$M_\odot$]	$R_{\rm WD}$ [$R_\odot$]
20713 (281)	8.150 (0.089)	0.705 (0.051)	0.01169 (0.00078)

of the physical structure of the disc, the inner and outer radii, can be easily inferred from these profiles as the Keplerian velocity increases with decreasing distance from the central object. The inner radius of the disc is determined from the maximum velocity, i.e. the point at which the emission drops to the continuum level; also known as the Full Width Zero Intensity (FWZI). We define the maximum red/blue-shifted velocities to represent the red/blue inner edges of the disc. The outer radius can be estimated from the peak separation in the double peaked profile. These observationally derived radii, $R_{\rm obs}$, relate to the true radii, R, via $R_{\rm obs} = R \sin^2 i$, where i is the inclination of the disc. This method was used by Gänsicke et al. (2006) to derive the observed inner and outer radii of SDSS J1228+1040 to be $\simeq 0.64\,R_\odot$ and $\simeq 1.2\,R_\odot$, respectively.

A departure from the symmetric double-peaked profile can reveal information about the physical structure of the disc, as demonstrated by Steeghs & Stehle (1999) for the occurence of spiral shocks in the disc (Steeghs et al. 1997; Steeghs 1999). An eccentric disc would generate an asymmetric double-peaked profile if viewed along the semi-minor axis, as there is an asymmetry in the amount of material

emitting red and blue-shifted light. We use this insight below to discuss the changes in the emission profiles seen in SDSS J1228+1040.

3.2 Variation of the calcium triplet profiles

The Ca II triplet in SDSS J1228+1040 has undergone an astonishing morphological evolution in the twelve years of observations (Figure 2). The three individual line profiles vary in the same manner and we therefore use the term "profile" to decribe their evolution. The initial spectra from 2003 and 2006 show a double-peaked profile indicative of a circumstellar disc with a red-dominated asymmetry. These observations were interpreted as emission from an eccentric disc with a non isotropic intensity distribution (Gänsicke et al. 2006). The maximum velocities (highest blue or red-shift) in the disc measured from the 2006 observations were found to be $\pm 560 \pm 10\,\mathrm{km\,s^{-1}}$.

As the profiles evolve, there is a general smooth progression from a red-dominated asymmetry to a blue-dominated one. Throughout this evolution the morphology of the peaks also changes, with the blue-shifted peak becoming stronger and sharper. In contrast, the red-shifted peak becomes shallower and weaker and extends to higher velocities, which can be seen first in the April 2009 observations. This extension into the red is clearest in the January 2011 spectrum with a maximum extension of $+780 \pm 10\,\mathrm{km\,s^{-1}}$. The clear, sharp cut-off of the red wing of the profile is a sudden change compared to the more gradual evolution in shape and implies that the red-shifted inner edge of the disc has moved inwards to smaller radii (i.e. higher velocities). From 2011–2015 the red wing decreases in extent, reducing the maximum velocity to $+670 \pm 10\,\mathrm{km\,s^{-1}}$, accompanied by an increase in strength, showing a clear reappearance of the red peak. Overall, the profile shifts to longer wavelengths, with the blue edge moving from $-560 \pm 10\,\mathrm{km\,s^{-1}}$ in July 2006 to $-390 \pm 10\,\mathrm{km\,s^{-1}}$ in May 2015. The variation in the red and blue velocities imply an asymmetry in the inner disc edge, as a circular Keplerian orbit would produce identical red/blue velocities. In summary, the observed variations clearly show that the inner edge of the gaseous disc is not circular.

4 ADDITIONAL EMISSION LINES IN SDSS J1228+1040

In addition to the Ca II triplet, Gänsicke et al. (2006) reported emission of Fe II 5169 / 5197 Å, however these lines were too weak to resolve the shape of their profiles. By inspecting the averaged X-shooter UVB and VIS spectral arms, we clearly detected these Fe II lines, as well as additional lines of Fe II, Ca II, Mg I, Mg II, and O I. The rest wavelengths of these lines are listed in Table 3, and their profiles are shown in Figure 3. We cannot inspect the time-resolved evolution of these lines as they are very weak and correspondingly noisy in the individual spectra.

It is evident that the four different species have distinct intensity distributions across the disc, which lead to the observed variety of line profile shapes. The sharp blue peak in the Ca II triplet is observed only in Mg I 8806 Å and Ca II 8912, 8927 Å. Rather surprisingly, the Ca H & K lines are different in shape to the Ca II triplet, with a broad profile, much weaker in strength, and no clear asymmetry in the blue edge. They do, however, possibly show an extension to the red similar to the Ca II triplet, although the signal-to-noise ratio of the individual observations makes the presence of such an extension uncertain. The O I lines at $\simeq$7774 and 8446 Å show a clear red-dominated asymmetric profile, which has the opposite shape of the Ca II triplet. The two emission profiles at $\sim$8245 (O I) and $\sim$9250 Å (O I and Mg II) are blended, extending over a larger wavelength range with a blurred structure.

Table 3. Additional emission lines detected in the average X-shooter spectrum (Figure 3) and the *HST* spectrum (Figure 4) of SDSS J1228+1040). The rest wavelengths were obtained from the NIST Atomic Spectra Database.

Ion	Rest wavelengths [Å]
Ca II	3933.66, 3968.47, 8498.02, 8542.09, 8662.14, 8912.07 8927.36
O I	7771.94, 7774.17, 7775.39, 8221.82, 8227.65, 8230.02, 8233.00, 8235.35, 8446.36, 8446.76, 8820.43, 9260.81, 9260.84, 9260.94, 9262.58, 9262.67, 9262.77, 9265.94, 9266.01
Mg I	8806.76
Mg II	2795.53, 2798.00, 2802.70, 4481.13, 4481.33, 7877.05, 7896.37, 8234.64, 9218.25
Fe II	4923.92, 5018.44, 5169.03, 5197.57, 5234.62, 5276.00, 5316.61, 5316.78

A number of emission profiles, such as Mg II 7896 Å, show sharp absorption features. These features are the photospheric absorption lines, which is also the case at 5041 and 5056 Å, where a Si II absorption doublet punctures the continuum.

We also show for reference the *HST* spectrum (Figure 4) obtained by Gänsicke et al. (2012) in the far and near ultraviolet spectral range. There are far more photospheric absorption lines in the ultraviolet compared to the optical range, but only one emission line; Mg II 2800 Å, which was first noted by Hartmann et al. (2011).

As done above for the Ca II triplet, we measured the maximum red/blue velocities of the emission profiles in the optical (where possible) to determine the radial extent of the different species. The additional emission features are orders of magnitude weaker than the strength of the Ca II lines (see Table 4), and it is therefore difficult to accurately determine the maximum red and blue-shifted velocities. However, the profiles have a similar FWZI in velocity space and as such we report the average velocities of the blue-most and red-most edge of the profiles as $\simeq 400\,\mathrm{km\,s^{-1}}$ and $\simeq 800\,\mathrm{km\,s^{-1}}$, respectively, which are consistent with those obtained for the Ca II triplet in all of the X-shooter observations so far. The similarity in the maximum and minimum velocities suggests that the emitting ions share a similar location of their inner disc edges. This is interesting to note as the line profiles differ in shape, implying different intensity distributions across the disc. Estimating an outer edge of the disc is much more difficult, as most of the additional emission profiles only have one clearly visible peak, and therefore a peak separation cannot be measured.

We compare the enlarged set of emission lines (Table 3)

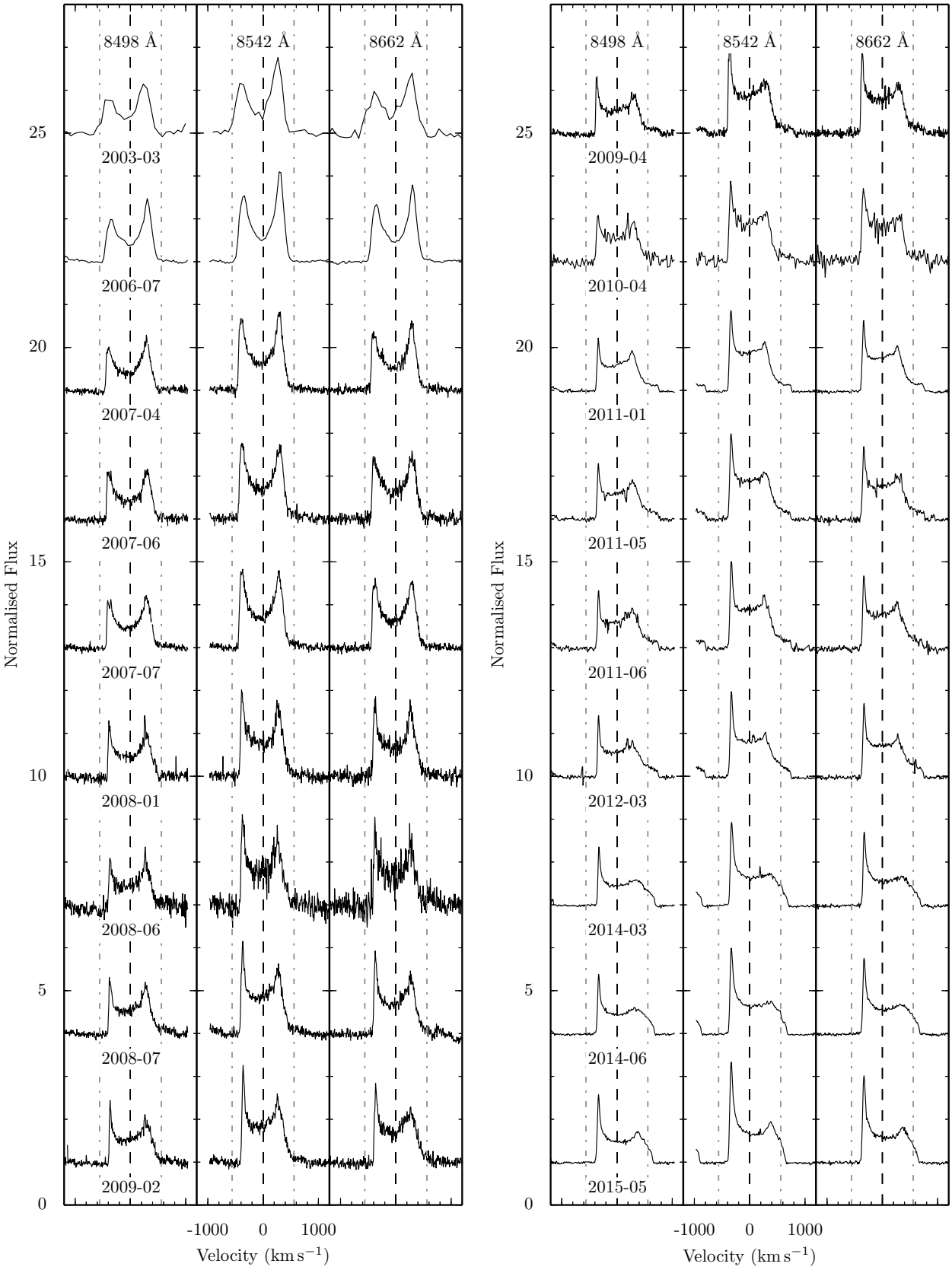

Figure 2. Time series of the continuum-divided Ca II triplet in SDSS J1228+1040 in velocity space. The series runs over twelve years with 18 epochs and depicts the change in the morphology of the line profiles. The dashed and dot-dashed lines indicate the zero velocity position, and the minimum and maximum velocities measured from the 2006 WHT data, respectively. The 2015 May profile is averaged from the X-shooter and UVES observations collected within several days of each other. The spectra are shifted in steps of three from the 2009 February (left) and 2015 May (right) observations.

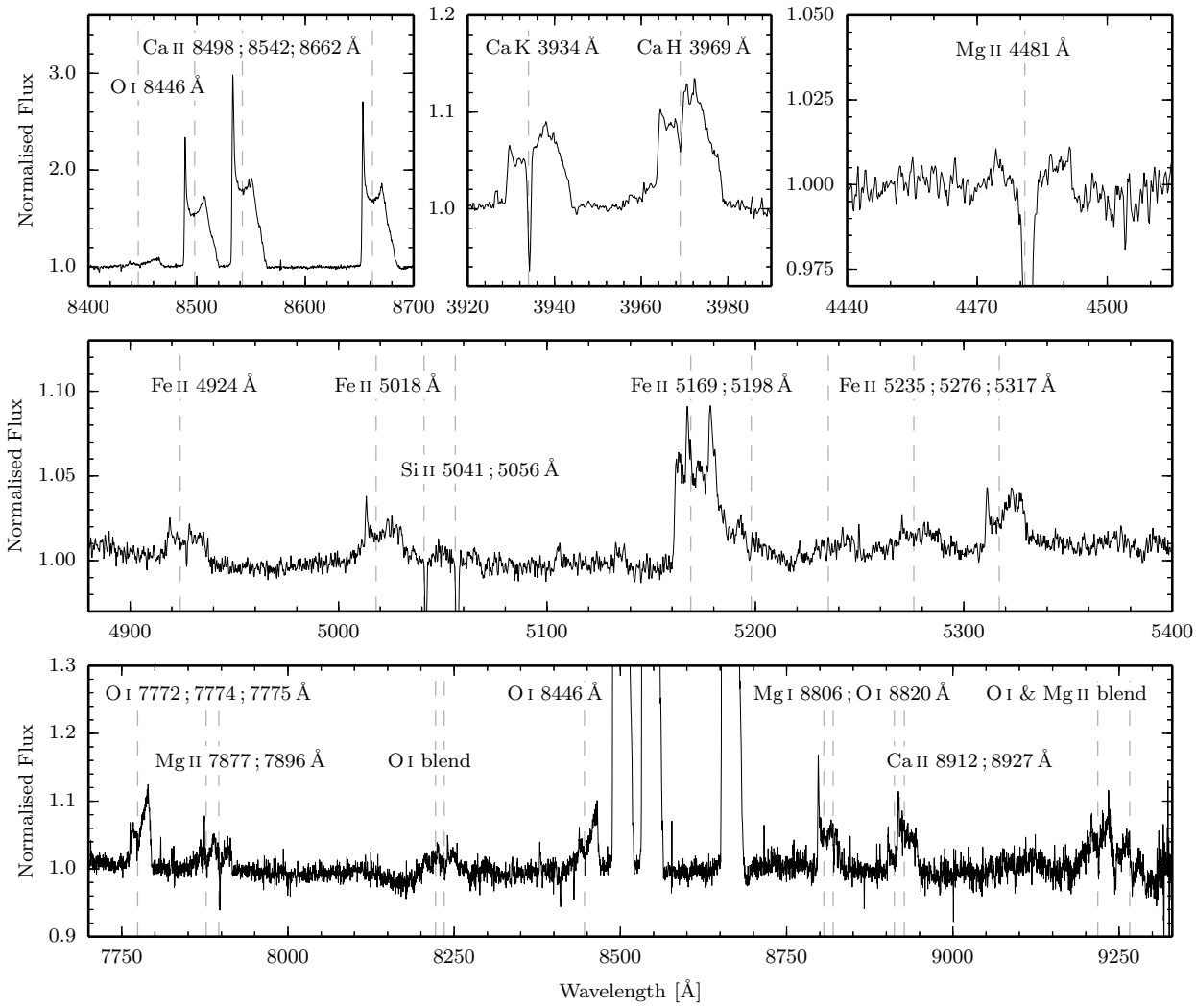
Ca II 8498 ; 8542; 8662 Å
O I 8446 Å
Ca K 3934 Å
Ca H 3969 Å
Mg II 4481 Å
Fe II 4924 Å
Fe II 5018 Å
Si II 5041 ; 5056 Å
Fe II 5169 ; 5198 Å
Fe II 5235 ; 5276 ; 5317 Å
O I 7772 ; 7774 ; 7775 Å
O I 8446 Å
Mg I 8806 ; O I 8820 Å
O I & Mg II blend
Mg II 7877 ; 7896 Å
O I blend
Ca II 8912 ; 8927 Å
Normalised Flux
Wavelength [Å]

Figure 3. The averaged, continuum-divided X-shooter spectrum of SDSSJ 1228+1040 reveals additional emission lines with a wide range of morphologies and strengths. The bottom panel contains the Ca II triplet, which extends far off of the plot, illustrating the extremely large dynamical range of the data. The ions that contribute to each profile are labelled in each panel, with dashed lines indicating their rest wavelengths. The regions labelled as blends contain multiple lines (see Table 3).

to the predictions from Non-Local Thermodynamic Equilibrium (NLTE) models of gaseous discs around white dwarfs (Hartmann et al. 2011). Each of the Ca and Mg lines detected in our X-shooter spectra are also present in the model of Hartmann et al. (2011), although they also predict other lines from these elements which we have not observed. These lines may lie below the detection threshold of our data, e.g. the predicted Mg I 5173 Å line is probably dominated by the emission of Fe II 5169 Å. We cannot compare our detections of Fe II or O I as these are not included in the calculations of Hartmann et al. (2011).

Hartmann et al. (2011) predict the Ca II triplet to be flanked by emission of C II 8700 Å. By comparison with the 2006 WHT spectra, the authors constrained the C abundance in the disc to less than 0.46 per cent by mass. Gänsicke et al. (2012) measured the C abundance of the debris accreted by SDSS J1228+1040 from *HST* UV spectra and found a mass fraction of 0.02 per cent, consistent with the non-detection of C emission in our deeper X-shooter spectra.

5 DOPPLER TOMOGRAPHY

While it is thought that the emission lines originate in a gaseous disc with an assumed Keplerian velocity field, the intensity distribution across the disc is not known. The smooth morphology variations of the Ca II triplet imply a gradual change in that distribution as viewed from Earth over the twelve years of observations, which is astonishing when compared to the orbital period of the material in the disc, which is of the order of a few hours.

One way of inducing the observed line profile variation could be the rotation (precession) of a fixed non-axisymmetric intensity structure. This has been proposed to explain some of the features observed in the emission line profiles seen at Be stars. These stars are rapidly rotating and

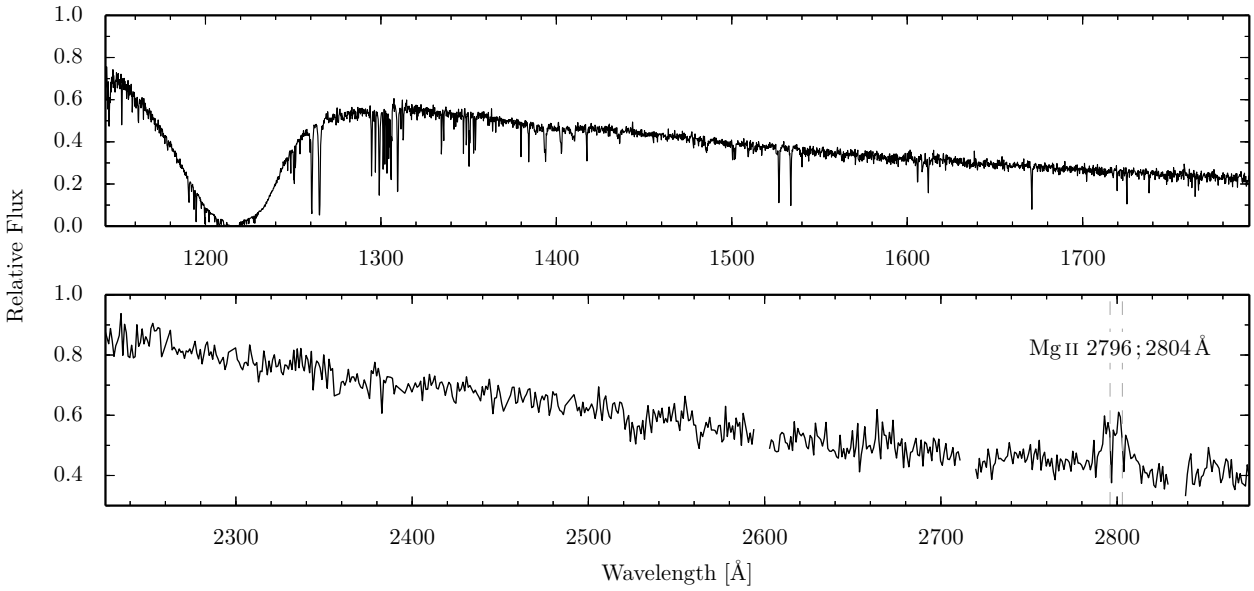

Figure 4. *HST* far (top) and near (bottom) ultraviolet observations of SDSS J1228+1040. The Mg II emission line is labelled.

Table 4. Equivalent widths (EW) of the emission features shown in Figures 3 & 4. The Ca II triplet are set in bold.

Identifier	Central wavelength [Å]	EW (error) [Å]
Mg II	2800	-7.9 (0.4)
Ca II	3934	-0.893 (0.007)
Ca II	3969	-1.485 (0.009)
Mg II	4481	-0.061 (0.002)
Fe II	4923	-0.243 (0.007)
Fe II	5018	-0.377 (0.008)
Fe II	5185	-1.60 (0.01)
Fe II	5235	-0.220 (0.009)
Fe II	5276	-0.478 (0.009)
Fe II	5317	-0.646 (0.007)
O I	7774	-2.20 (0.02)
Mg II	7877	-0.78 (0.02)
O I	8230	-0.71 (0.03)
O I	8446	-1.50 (0.02)
Ca II	**8498**	**-16.73 (0.03)**
Ca II	**8542**	**-23.45 (0.03)**
Ca II	**8662**	**-20.76 (0.03)**
Mg I, O I	8810	-1.73 (0.03)
Ca II	8920	-1.90 (0.03)
O I, Mg II	9234	-2.64 (0.05)

host circumstellar material in disc structures that frequently show long term variability (Okazaki 1991; Papaloizou et al. 1992; Okazaki 1997). Hanuschik et al. (1995) report line profiles of Fe II 5317 Å (see their Figures 8, 14, and 15) seen in Be stars which are remarkably similar to the Ca II triplet observations of SDSS J1228+1040.

To test the hypothesis of a fixed intensity structure, we fit the Ca II triplet line profile using the method of Doppler tomography. Doppler tomography is commonly employed to deduce the structure of discs in accreting binary systems (Marsh & Horne 1988; Steeghs & Stehle 1999, see Marsh 2001 for a review; in particular his Figure 3). Doppler tomography produces a fixed intensity map (or Doppler map) in velocity space that, for a given period of rotation, best replicates the observed line profiles across all available epochs under the following assumptions (Marsh 2001): 1) All points on the disc are equally visible at all times. 2) The flux from any point fixed in the rotating frame is constant in time. 3) All motion is parallel to the orbital plane. 4) The intrinsic width of the profile from any point is negligible. The Doppler map can also be used to reproduce an emission line profile for a given epoch by reducing the 2D intensity map in velocity space to a 1D intensity distribution in the velocity projected along the corresponding line of sight. Doppler maps are useful tools to study disc structure as the conversion from coordinate space to velocity space is non-unique and multiple intensity profiles across a disc structure can produce the same emission profile.

We used the 18 Ca II triplet profiles collected for SDSS J1228+1040 to produce Doppler maps with a range of trial periods spanning 24.64 years (9000 days) to 68.45 years (25000 days) with increments of 500 days. We would not expect a period much shorter than $\simeq 25$ years; otherwise the disc would have precessed $\geqslant 180^\circ$, producing emission lines that are the reflection of the 2003 March observation.

Doppler maps with periods between $\sim$24–30 years ($\sim$9000–11000 days) appear very similar with only slight changes in the shape of the intensity distribution. However, for periods longer than 30 years the maps of the disc become elongated or stretched, generating discontinuous changes in velocity not expected for Keplerian orbits. Maps with periods longer than 30 years also generate emission profiles with an additional peak in each of the components of the Ca II triplet, which are not observed here or in other systems with Ca II emisison (see Section 7). We therefore adopt a period in between 24–30 years; 27.4 years (10000 days) and the Doppler map generated with this period is shown in Figure 5. We also show a trailed spectrogram generated from the Doppler map over one full 27.4 years cycle (Figure 6). These

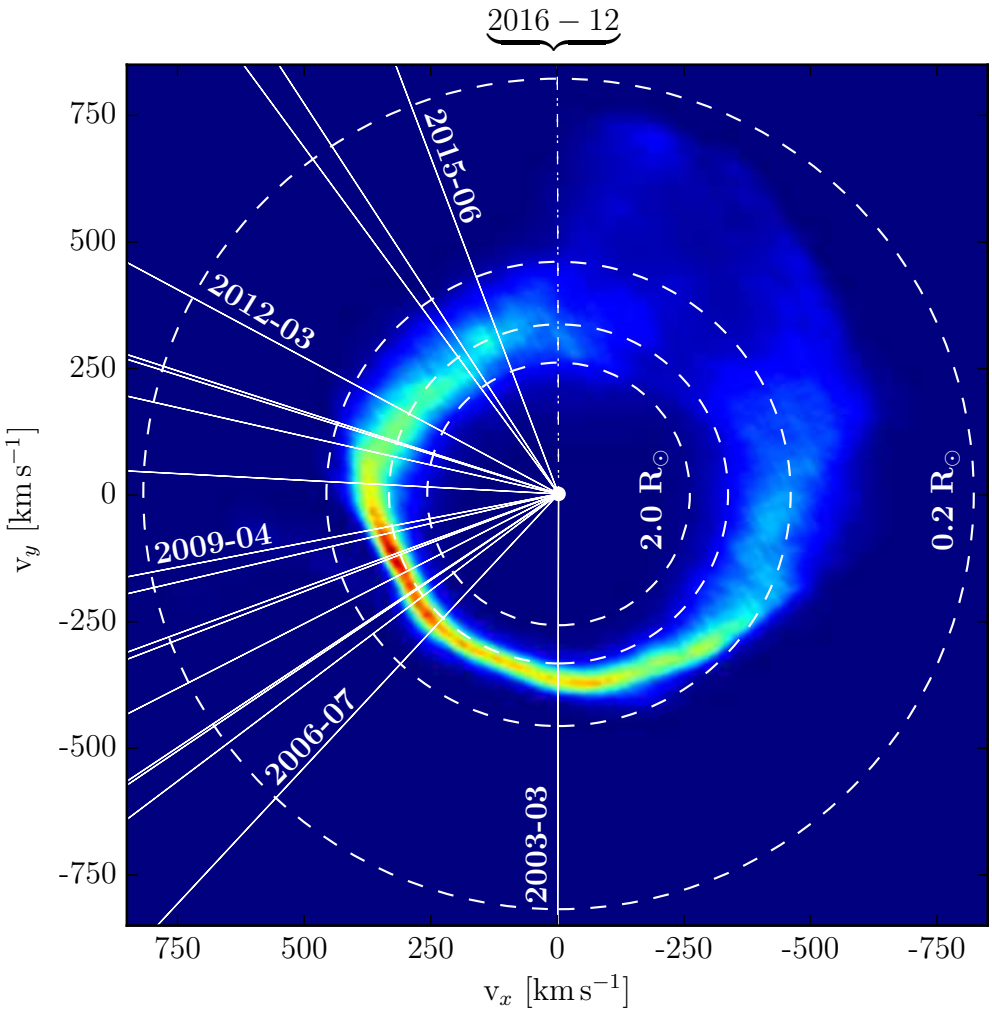

Figure 5. An intensity distribution in velocity space of the Ca II triplet, which models the line profiles observed in SDSS J1228+1040 obtained from Doppler tomography. The white dwarf is located at the origin of the map where the lines intersect as a solid white circle. The solid white lines represent the epoch and line of sight for each observation from March 2003 to May 2015 and the dot-dashed white line indicates when we expect the Ca II triplet to return to a morphology similar to that observed in 2003 (December 2016). The resulting profile would be a reflection of the first observation, assuming a precession period of $\simeq 27$ years. The dashed white circles indicate the location of material in a Keplerian orbit around SDSS J1228+1040, with observed orbital radii ($R \sin^2 i$) of 0.2, 0.64, 1.2 and 2 $R_\odot$, with the largest circle (highest velocities) corresponding to 0.2 $R_\odot$, and the smallest circle (lowest velocities) to 2$R_\odot$.

predictions will be compared against future spectroscopy of the Ca II triplet in SDSS J1228+1040.

The outer edge of the intensity structure corresponds to the highest velocities and hence the inner edge of the disc in coordinate space. The inner edge is clearly asymmetric, with a large dispersed region and a narrow intense strip related to the large red-shifted velocities and the sharp blue-shifted peak seen in the emission profiles, respectively.

During the 2003–2008 observations, the dispersed and narrow regions discussed above have projected velocities along the line of sight which are significantly reduced, increasing the central strength near zero velocity rather than the extremes of the profile. The dashed lines in Figure 5 represent circular orbits in velocity space, underlining that the Doppler image of SDSS J1228+1040 is highly non-circular, which agrees with our qualitative description of the line profiles in Section 3. Further, this non-circularity cannot be described well as a single eccentricity, but rather by a changing eccentricity as a function of radius.

From the Doppler map we reconstructed the emission features observed in order to check for self consistency (Figure 7). The line profiles generated from the Doppler map fit remarkably well for most epochs, although the sharpness of the red and blue-shifted peaks seen between 2008–2010 are not totally replicated. The inability to fully reconstruct all details of the observed emission profiles may suggest that

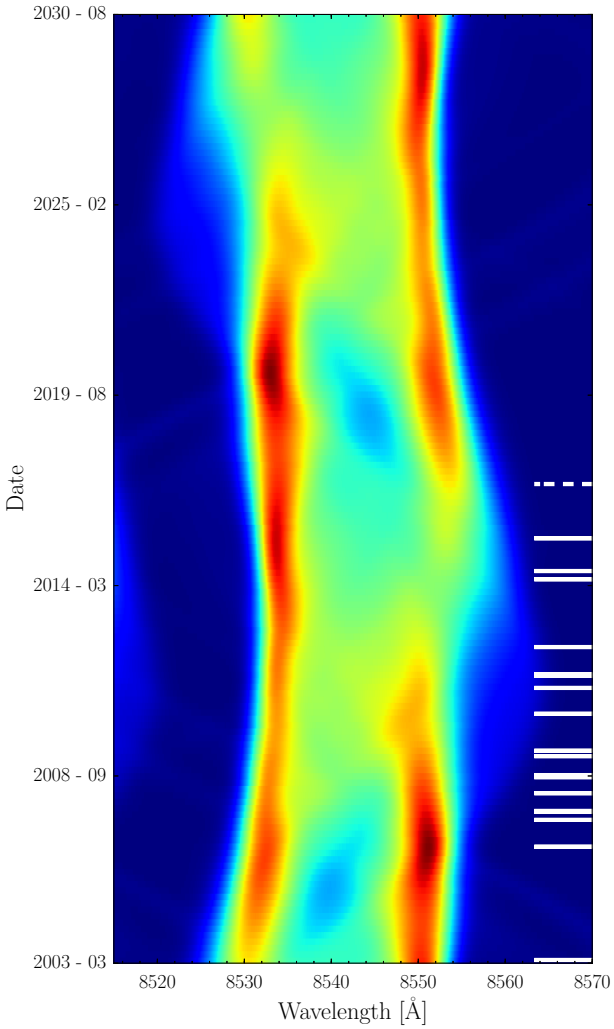

Figure 6. A trailed spectrogram generated from the Doppler map in Figure 5 over one full 27.4 years cycle. The solid and dashed white tabs indicate the position in the spectrogram where we have observed data, and the predicted halfway point respectively.

one or more of the assumptions underlying the method of Doppler tomography are not fulfilled in SDSS J1228+1040, e.g. there could be additional short term variability in the system.

An additional note regarding the interpretation of the Doppler map is that it depicts only the intensity distribution of Ca II. The difference in morphology between the Ca II triplet and other ions, such as O I (see Section 3) suggests that these elements have different intensity distributions across the disc. Therefore Doppler maps of the emission lines of other ions in combination with that of Ca II could reveal additional information on the physical conditions (e.g. density, temperature) within the disc, if time-series spectroscopy with a sufficient signal-to-noise ratio is obtained.

6 A PRECESSING DISC?

We find that the data and the velocity map shown in Figure 5 are largely consistent with a constant non-axisymmetric intensity structure that precesses around the white dwarf, resulting in a periodically varying projection into the observed emission line profiles. The precession and the structure of the disc could be explained by several scenarios, which are not necessarily mutually exclusive:

1) We are observing a young, eccentric disc that has only recently formed from the tidal disruption of an asteroid. If only gravitational forces are considered, the asteroid is disrupted and forms a broken, highly-eccentric ring of debris around the white dwarf, the majority of which is located outside of the tidal disruption radius (Veras et al. 2014). Adding radiation forces causes the particles in the disc to spread inwards towards the white dwarf (on time-scales determined by their size), eventually circularising (Veras et al. 2015). However, the time-scale on which a debris disc circularises is currently poorly known due to the complexity of the forces (e.g. radiation, gas drag) upon and the interactions (e.g. collisions) between the particles. If the circularisation time-scale is significantly shorter than the twelve years spanned by our observations, we would expect the asymmetry in the emission features to have evolved towards a constant, symmetric double-peaked line profile.

2) Precession due to general relativity. General relativistic effects will cause an eccentric orbit to precess over one full orbit on a period P_ω that is given by

$$P_\omega \approx 84.98 \text{ yr} \left(\frac{M}{0.70\text{M}_\odot}\right)^{-3/2} \left(\frac{a}{1.00\text{R}_\odot}\right)^{5/2} \left(1-e^2\right) \quad (1)$$

where M is the mass of the central star and a is the semi-major axis of the orbit (see Veras 2014 for details). In the limit of small eccentricities we can ignore the term $(1 - e^2)$. By adopting $M_{\text{wd}} = 0.7\,\text{M}_\odot$, we find precession periods of 1.54, 27.8 and 134 years for orbits with semi-major axes of 0.2, 0.64 $\text{R}_\odot$ and 1.2 $\text{R}_\odot$ respectively, i.e. the period of precession has a strong radial dependence.

General relativistic precession is intrinsic to any orbital mechanics, and furthermore the period of 27.8 years for an orbit at 0.64 $\text{R}_\odot$ is close to the period range deduced from our Doppler maps $\simeq$24–30 years. Therefore it is expected that general relativity should have a significant contribution to the variability observed in this system. The radial dependence of the precession period due to general relativity will cause collisions among the dust particles on different orbits, which is a possible mechanism for generating the observed gaseous component of the debris disc. These collisions would also act to dampen the eccentricity into a circular orbit, where production of gas due to general relativistic precession would eventually cease. It is worth noting that the Doppler map (inherently) does not display the radial dependence of the general relativistic precession, which may be dampened by other forces (e.g. gas pressure effects in the disc).

3) An external perturber outside the disc inducing both the eccentricity and precession. The flyby of a body orbiting on an eccentric orbit would perturb the orbits of the particles in the disc. We have performed some numerical N-body simulations to determine the effect of an external perturber

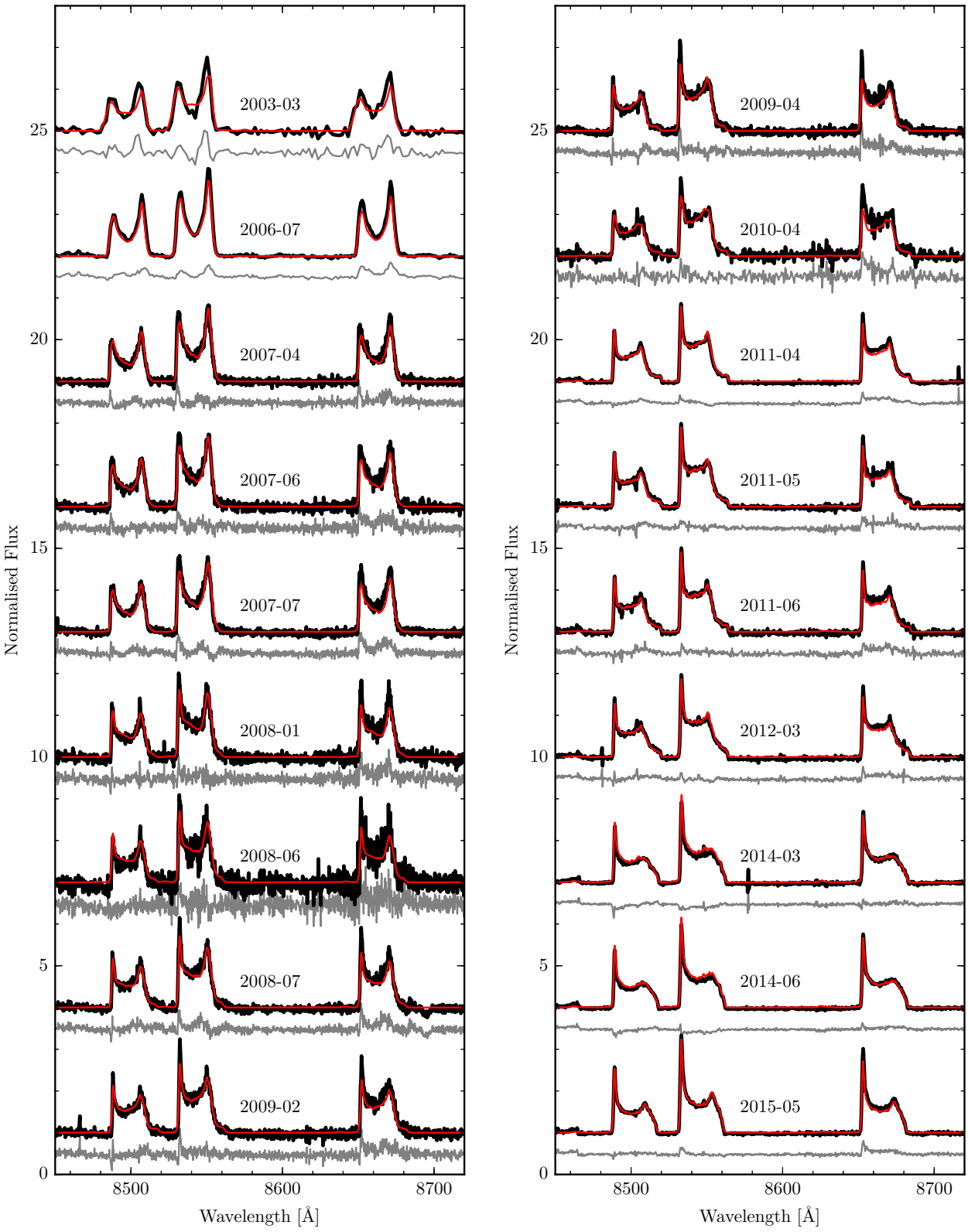

Figure 7. The continuum-divided Ca II triplet line profiles (black) for SDSS J1228+1040 in chronological order (as in Figure 2) reconstructed (red) using the Doppler map in Figure 5 with residuals (grey). The spectra are shifted in steps of three from the 2009 February (left) and 2015 May observations (right).

on circular rings of particles located at about one Solar radius from the white dwarf. Because the asymptotic giant branch progenitor of SDSS J1228+1040 had a radius of at least 2.5–3.0 au, surviving planet-sized perturbers must now have a semimajor axis exceeding 3–11 au (see, e.g. Figure 10 of Mustill & Villaver 2012). Consequently, a perturber's current orbital period must be at least several years, which covers multiple observations from Figure 7, in particular during the years 2007–2008, where the observations are closely spaced. We therefore adopted a perturber semimajor axis of 5 au, with masses ($10^0 - 10^4 M_\oplus$) and eccentricities (0.990–0.998 - a realistic possibility; see Debes & Sigurdsson 2002; Veras et al. 2013; Voyatzis et al. 2013; Mustill et al. 2014; Bonsor & Veras 2015; Veras & Gänsicke 2015) in ranges that might produce an observable eccentricity change in the ring. Smaller mass perturbers would have to approach so close to the ring particles to potentially be in danger of tidally disrupting.

Each simulation contained 210 massless ring particles, and spanned one close encounter. The white dwarf mass was set at $0.705\,M_\odot$, and the particles were equally partitioned into seven rings at distances of $\{0.6, 0.7, 0.8, 0.9, 1.0, 1.1, 1.2\,R_\odot\}$. We uniformly distributed the initial mean anomalies of the particles within each ring.

In every case changes in ring particle eccentricity occurred only within a few hours of a close encouter. During the remainder of the orbit, there was no eccentricity change. Therefore, in-between encounters (spanning several years), the geometry of the disc did not change, which is at odds with the observations from Figure 7. This mismatch would also hold true for perturbers with initially greater semimajor axes.

4) The disc induces its own eccentricity and precession. Statler (2001) has shown that an eccentric flat fluid disc can precess due to the pressure gradient generated within the disc. Figure 3 from Statler (2001) shows line profiles that are similar in morphology to that of SDSS J1228+1040 (see Section 3). In contrast to these simulations of purely fluid discs, the gaseous discs that we have observed are coupled to dust grains. Kinnear (2011) finds a typical gas mass, $M_{\rm gas}$, of $\sim 10^{19}$ g. Estimates of the dust mass, $M_{\rm dust}$, range from 10^{19} to 10^{24} g, from disc models that reproduce the observed infrared excess in systems with dusty discs (see, Jura et al. 2007; Jura 2008; Reach et al. 2009), i.e. $M_{\rm gas} \leqslant M_{\rm dust}$ and as such we can not assume the disc is dominated by the gaseous component. Finally, it is worth noting that Ogilvie (2001) finds that the eccentricity in a disc will dissipate on the viscous time-scale, which we estimate to be $\simeq$ 5-20 years (Section 6), i.e. similar to our observational baseline. Given that the eccentricity in SDSS J1228+1040 persists over this time scale, self-induction seems unlikely.

Of the different scenarios outlined above, a young eccentric disc that precesses due to general relativity appears to be the most natural scenario that can describe our observations. We would also expect this phase to be fairly short-lived, which would explain the rarity of detected gaseous debris disc components. Assuming the adopted precession period of 27.4 years, the system is expected to reach half way through the precession cycle in December 2016, i.e. we would expect a Ca II triplet morphology that is the reflection of the March 2003 observations. In the next section we discuss the variability seen in other gaseous discs around white dwarfs and the possible generation mechanisms for these systems.

7 DISCUSSION

Besides the observations of SDSS J1228+1040 presented here, changes in the Ca II emission lines have been reported for two other systems with a gaseous disc; SDSS J0845+2258, and SDSS J1617+1620 (Wilson et al. 2014, 2015). In SDSS J0845+2257 the Ca II profiles evolved in shape from a strong, red-dominated asymmetry to a slight, blue-dominated symmetric profile over a time-scale of ten years; similar to the overall variation seen in the Ca II triplet of SDSS J1228+1040. In contrast, morphological changes in the line profile were not apparent in SDSS J1617+1620, where the Ca II emission lines from the gaseous disc remained symmetric (suggesting an axisymmetric intensity pattern) and decreased in strength, eventually disappearing within eight years (Wilson et al. 2014).

There are four other white dwarfs known to host a gaseous disc: SDSS J104341.53+085558.2 (henceforth SDSS J1043+0855), SDSS J073842.56+183509.6 (henceforth SDSS J0738+1835), SDSS J0959–0200, and HE 1349–2305. Of these four systems only SDSS J1043+0855 and SDSS J0738+1835 have multi-epoch spectroscopy. SDSS J1043+0855 shows variability similar to SDSS J1228+1040 although only a handful of epochs are available so far (Manser et al. 2016). In contrast, SDSS J0738+1835 shows no change in the shape or strength of the Ca II triplet over a period of six years (Gänsicke 2011; Dufour et al. 2012). However, with only three epochs, more data is needed to confirm the steady state of SDSS J0738+1835. The emission lines in HE 1349–2305 show a large asymmetry similar to the systems with a morphological variation (SDSS J1228+1040, SDSS J1043+0855 and SDSS J0845+2257), and therefore this star would be an ideal candidate for follow up observations to detect variability (Melis et al. 2012). The Ca II triplet observed at SDSS J0959–0200 is much narrower and weaker than that of the other six systems, indicating a low inclination of the disc with respect to the line of sight (Farihi et al. 2012). Finally, Guo et al. (2015) recently identified the candidate gas disc at SDSS J114404.74+052951.6 which has Ca II emission similar that of SDSS J0959–0200. The system also shows infrared excess attributed to a dusty debris disc, but the Ca II emission lines are extremely weak, and follow up observations are needed to confirm the presence of a gaseous component.

The gaseous component of a debris disc will accrete onto the white dwarf, and without a sustained generation mechanism will dissipate over the viscous time-scale, which can be estimated using equation 2 from Metzger et al. (2012). The major uncertainty is the value of α, the accretion disc viscosity parameter (Shakura & Sunyaev 1973). King et al. (2007) suggest $0.1 \leqslant \alpha \leqslant 0.4$ for a thin fully ionised disc. Given that the metallic gas is ionised to a high degree, it is plausible to adopt this range for α, which leads to viscous time-scales of 5–20 years for a typical white dwarf mass. These time-scales match the disappearance of the Ca II lines observed in SDSS J1617+1620 discussed above.

We calculated the equivalent width of the Ca II triplet

Table 5. Equivalent width measurements of the Ca II triplet in SDSS J1228+1040.

Date	Equivalent width [Å]
2003–03	-60 (7)
2006–07	-69 (2)
2007–04	-61 (2)
2007–06	-63 (2)
2007–07	-63 (2)
2008–01	-60 (2)
2008–06	-54 (2)
2008–07	-60 (2)
2009–02	-58 (2)
2009–04	-62 (2)
2010–04	-67 (1)
2011–01	-57 (1)
2011–05	-60 (1)
2011–06	-59 (1)
2012–03	-56 (1)
2014–03	-50 (1)
2014–06	-52 (1)
2015–05	-57 (1)

for SDSS J1228+1040 for each epoch (Table 5), and do not detect any significant decrease, suggesting that; 1) the gaseous discs in SDSS J1228+1040 and SDSS J0845+2257 are being sustained by ongoing gas production, and 2) there may be multiple pathways to generate a gaseous disc given that there are clear differences in the type of variability seen in these three systems and SDSS J1617+1620.

From Section 6, a natural scenario to explain the morphology variation is that of a young eccentric disc that precesses due to general relativity with the radial dependence of the precession period resulting in ongoing collisional gas production that ceases once the disc circularises. This scenario allows for gas generation, while not being mutually exclusive with the observations of SDSS J1617+1620, which would be better explained by a transient event such as a secondary asteroid impact onto a pre-existing, circularised disc (Jura 2008). Such an asteroid impact would generate an initial quantity of gas that would subsequently dissipate over the viscous time-scale.

The relatively short-lived transient nature of these gas generation mechanisms also explains why there are systems with accretion rates much larger than that of SDSS J1228+1040, such as PG 0843+516 and GALEX 1931+0117, which do not show any sign of a gaseous disc (Gänsicke et al. 2012). We expect that debris discs with no detectable gaseous component are largely circularised.

8 CONCLUSIONS

We report the pronounced morphology changes of the Ca II triplet at SDSS J1228+1040 which we have modelled using the method of Doppler tomography. This procedure produced a non-axisymmetric intensity map in velocity space of the Ca II triplet, which we have interpreted as a precessing disc with a period in the range 24–30 years. We also detected additional emission lines in the averaged X-shooter spectra of SDSS J1228+1040, increasing the number of observed gaseous elements in this system to four. The variation in shape between the emission features of different ions is a clear indication that the intensity distribution in the disc for each ion is not the same. With time-resolved spectroscopy and sufficient signal-to-noise, Doppler tomography of the additional line profiles (such as O I 7774, 8446 Å) may reveal information about the physical properties in the disc (e.g density and temperature distributions).

The gaseous component of debris discs are a tracer of dynamical activity in these systems. Four of the five gaseous discs with time-resolved observations over time-scales of years show variability, and small-number statistics so far suggest that the dynamic variability of the gaseous discs themselves is the the norm rather than the exception.

ACKNOWLEDGEMENTS

We thank the referee for their helpful comments and suggestions for improving this manuscript. The research leading to these results has received funding from the European Research Council under the European Union's Seventh Framework Programme (FP/2007-2013) / ERC Grant Agreement n. 320964 (WDTracer). We would like to thank Yan-Ping Chen and Scott Trager for sharing their X-shooter telluric template library. TRM acknowledges support from the Science and Technology Facilities Council (STFC), grant ST/L000733/1. SGP acknowledges financial support from FONDECYT in the form of grant number 3140585. CJM would like to thank Mark Hollands for his help with Figure 1.

Based on observations made with ESO Telescopes at the La Silla Paranal Observatory under programme IDs: 079.C-0085, 081.C-0466, 082.C-0495, 087.D-0139, 088.D-0042, 093.D-0426, 095.D-0802, 192.D-0270, 383.C-0695, 386.C-0218, 595.C-0650. This work has made use of observations from the SDSS-III, funding for which has been provided by the Alfred P. Sloan Foundation, the Participating Institutions, the National Science Foundation, and the U.S. Department of Energy Office of Science. The SDSS-III web site is http://www.sdss3.org/. Based on observations made with the NASA/ESA HST, obtained at the Space Telescope Science Institute, which is operated by the Association of Universities for Research in Astronomy, Inc., under NASA contract NAS 5-26555. These observations are associated with program 11561. Based on observations made with the WHT operated on the island of La Palma by the Isaac Newton Group in the Spanish Observatorio del Roque de los Muchachos of the Instituto de Astrofsica de Canarias.

REFERENCES

Abazajian K. N., et al., 2009, ApJS, 182, 543
Ahn C. P., et al., 2014, ApJ, 211, 17
Bergfors C., Farihi J., Dufour P., Rocchetto M., 2014, MNRAS, 444, 2147
Bonsor A., Veras D., 2015, MNRAS, 454, 53
Brinkworth C. S., Gänsicke B. T., Marsh T. R., Hoard D. W., Tappert C., 2009, ApJ, 696, 1402
Brinkworth C. S., Gänsicke B. T., Girven J. M., Hoard D. W., Marsh T. R., Parsons S. G., Koester D., 2012, ApJ, 750, 86
Chen Y.-P., Trager S. C., Peletier R. F., Lançon A., Vazdekis A., Prugniel P., Silva D. R., Gonneau A., 2014, A&A, 565, A117

Debes J. H., Sigurdsson S., 2002, ApJ, 572, 556
Debes J. H., Hoard D. W., Wachter S., Leisawitz D. T., Cohen M., 2011, ApJS, 197, 38
Debes J. H., Walsh K. J., Stark C., 2012, ApJ, 747, 148
Dekker H., D'Odorico S., Kaufer A., Delabre B., Kotzlowski H., 2000, in Iye M., Moorwood A. F., eds, Society of Photo-Optical Instrumentation Engineers (SPIE) Conference Series Vol. 4008, Optical and IR Telescope Instrumentation and Detectors. pp 534–545
Dufour P., Kilic M., Fontaine G., Bergeron P., Lachapelle F., Kleinman S. J., Leggett S. K., 2010, ApJ, 719, 803
Dufour P., Kilic M., Fontaine G., Bergeron P., Melis C., Bochanski J., 2012, ApJ, 749, 6
Eisenstein D. J., et al., 2011, AJ, 142, 72
Farihi J., Zuckerman B., Becklin E. E., 2008, ApJ, 674, 431
Farihi J., Jura M., Zuckerman B., 2009, ApJ, 694, 805
Farihi J., Gänsicke B. T., Steele P. R., Girven J., Burleigh M. R., Breedt E., Koester D., 2012, MNRAS, 421, 1635
Freudling W., Romaniello M., Bramich D. M., Ballester P., Forchi V., García-Dabló C. E., Moehler S., Neeser M. J., 2013, A&A, 559, A96
Gänsicke B. T., 2011, in Schuh S., Drechsel H., Heber U., eds, American Institute of Physics Conference Series Vol. 1331, American Institute of Physics Conference Series. pp 211–214 (arXiv:1101.3946), doi:10.1063/1.3556202
Gänsicke B. T., Marsh T. R., Southworth J., Rebassa-Mansergas A., 2006, Science, 314, 1908
Gänsicke B. T., Marsh T. R., Southworth J., 2007, MNRAS, 380, L35
Gänsicke B. T., Koester D., Marsh T. R., Rebassa-Mansergas A., Southworth J., 2008, MNRAS, 391, L103
Gänsicke B. T., Koester D., Farihi J., Girven J., Parsons S. G., Breedt E., 2012, MNRAS, 424, 333
Graham J. R., Matthews K., Neugebauer G., Soifer B. T., 1990, ApJ, 357, 216
Gunn J. E., et al., 2006, AJ, 131, 2332
Guo J., Tziamtzis A., Wang Z., Liu J., Zhao J., Wang S., 2015, ApJ, 810, L17
Hanuschik R. W., Hummel W., Dietle O., Sutorius E., 1995, A&A, 300, 163
Hartmann S., Nagel T., Rauch T., Werner K., 2011, A&A, 530, A7
Hoard D. W., Debes J. H., Wachter S., Leisawitz D. T., Cohen M., 2013, ApJ, 770, 21
Horne K., Marsh T. R., 1986, MNRAS, 218, 761
Jura M., 2003, ApJ Lett., 584, L91
Jura M., 2008, AJ, 135, 1785
Jura M., Young E. D., 2014, Annual Review of Earth and Planetary Sciences, 42, 45
Jura M., Farihi J., Zuckerman B., 2007, ApJ, 663, 1285
Jura M., Farihi J., Zuckerman B., 2009, AJ, 137, 3191
Kilic M., von Hippel T., Leggett S. K., Winget D. E., 2006, ApJ, 646, 474
King A. R., Pringle J. E., Livio M., 2007, MNRAS, 376, 1740
Kinnear T., 2011, Master's thesis, University of Warwick
Koester D., 1987, ApJ, 322, 852
Koester D., Provencal J., Shipman H. L., 1997, A&A, 320, L57
Koester D., Gänsicke B. T., Farihi J., 2014, A&A, 566, A34
Manser C. J., Gänsicke B. T., Koester D., 2016, in prep
Marsh T. R., 2001, in Boffin H. M. J., Steeghs D., Cuypers J., eds, Lecture Notes in Physics, Berlin Springer Verlag Vol. 573, Astrotomography, Indirect Imaging Methods in Observational Astronomy. p. 1 (arXiv:astro-ph/0011020)
Marsh T. R., Horne K., 1988, MNRAS, 235, 269
Melis C., et al., 2012, ApJ Lett., 751, L4
Metzger B. D., Rafikov R. R., Bochkarev K. V., 2012, MNRAS, 423, 505
Mustill A. J., Villaver E., 2012, ApJ, 761, 121
Mustill A. J., Veras D., Villaver E., 2014, MNRAS, 437, 1404
Ogilvie G. I., 2001, MNRAS, 325, 231
Okazaki A. T., 1991, PASJ, 43, 75
Okazaki A. T., 1997, A&A, 318, 548
Papaloizou J. C., Savonije G. J., Henrichs H. F., 1992, A&A, 265, L45
Rafikov R. R., 2011, MNRAS, 416, L55
Reach W. T., Lisse C., von Hippel T., Mullally F., 2009, ApJ, 693, 697
Rocchetto M., Farihi J., Gänsicke B. T., Bergfors C., 2015, MNRAS, 449, 574
Shakura N. I., Sunyaev R. A., 1973, A&A, 24, 337
Smee S. A., et al., 2013, AJ, 146, 32
Statler T. S., 2001, AJ, 122, 2257
Steeghs D., 1999, PhD thesis, University of St.Andrews
Steeghs D., Stehle R., 1999, MNRAS, 307, 99
Steeghs D., Harlaftis E. T., Horne K., 1997, MNRAS, 290, L28
Veras D., 2014, MNRAS, 442, L71
Veras D., Gänsicke B. T., 2015, MNRAS, 447, 1049
Veras D., Mustill A. J., Bonsor A., Wyatt M. C., 2013, MNRAS, 431, 1686
Veras D., Leinhardt Z. M., Bonsor A., Gänsicke B. T., 2014, MNRAS, 445, 2244
Veras D., Leinhardt Z. M., Eggl S., Gänsicke B. T., 2015, MNRAS, in press
Vernet J., et al., 2011, A&A, 536, A105
Voyatzis G., Hadjidemetriou J. D., Veras D., Varvoglis H., 2013, MNRAS, 430, 3383
Wilson D. J., Gänsicke B. T., Koester D., Raddi R., Breedt E., Southworth J., Parsons S. G., 2014, MNRAS, 445, 1878
Wilson D. J., Gänsicke B. T., Koester D., Toloza O., Pala A. F., Breedt E., Parsons S. G., 2015, MNRAS, 451, 3237
Xu S., Jura M., 2014, ApJ, 792, L39
Xu S., Jura M., Pantoja B., Klein B., Zuckerman B., Su K. Y. L., Meng H. Y. A., 2015, ApJ Lett., 806, L5
Zuckerman B., Becklin E. E., 1987, Nat, 330, 138
Zuckerman B., Koester D., Melis C., Hansen B. M., Jura M., 2007, ApJ, 671, 872

This paper has been typeset from a TEX/LATEX file prepared by the author.